Powder Technology 415 (2023) 118145

Contents lists available at ScienceDirect

Powder Technology

journal homepage: www.journals.elsevier.com/powder-technology

Investigation of magnetite particle characteristics in relation to crystallization pathways

Andreas Bogen Kristiansen [a], Nathan Church [b], Seniz Ucar [a,*]

[a] Department of Chemical Engineering, Norwegian University of Science and Technology, Sem Sælandsvei 4, 7491 Trondheim, Norway
[b] Department of Geoscience and Petroleum, Norwegian University of Science and Technology, S. P. Andersens veg 15a, 7031 Trondheim, Norway

HIGHLIGHTS

- Magnetite nanopowder is obtained via coprecipitation through a multistep reaction.
- Ionic and non-ionic PEG additives affect the final particle properties.
- Regulatory roles of additives are correlated with their effects on reaction kinetics.
- Multistep pathways can be used for green synthesis of magnetite nanopowder.

GRAPHICAL ABSTRACT

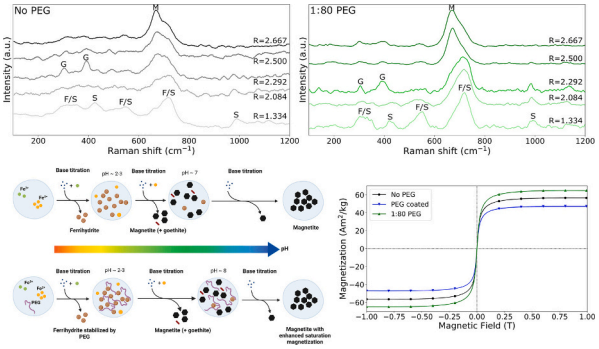

ARTICLE INFO

Keywords:
Magnetite nanoparticles
Bioinspired synthesis
Supersaturation
Phase transformation
Coprecipitation

ABSTRACT

Intense research on magnetite nanoparticles and their synthesis methods stems from being ideal candidates for a variety of technological applications that use their unique magnetic properties. Strict control of the magnetic properties of magnetite for its most efficient use can be acquired by controlling particle characteristics such as size, shape and crystallinity. Bioinspired pathways that follow multistep crystallization routes, combined with the use of regulatory additives offer versatile synthesis platforms for the precipitation of tailored magnetite nanoparticles. However, our ability to control particle characteristics is limited by our understanding of the crystal formation pathways. Here we show that by using bioinspired coprecipitation and introducing polyethylene glycol (PEG) as an additive, superparamagnetic magnetite particles with enhanced magnetization can be synthesized. The bioinspired coprecipitation method allows stepwise precipitation of metastable iron oxide phases prior to magnetite formation via slow titration of a base into a solution of iron precursors. The regulatory roles of ionic and non-ionic PEG additives on particle characteristics are correlated with their effects on the multistep particle formation pathway and the kinetics of magnetite crystallization via phase transformation.

* Corresponding author.
E-mail addresses: andreas.b.kristiansen@gmail.com (A.B. Kristiansen), nathan.church@ntnu.no (N. Church), seniz.ucar@ntnu.no (S. Ucar).

https://doi.org/10.1016/j.powtec.2022.118145
Received 8 September 2022; Received in revised form 16 November 2022; Accepted 1 December 2022
Available online 5 December 2022

1. Introduction

Magnetite (Fe_3O_4) is a naturally occurring iron oxide commonly found in both biological and geological systems. It is the most magnetic material found naturally on Earth, and led humans to the discovery of the fascinating world of magnetism already in ancient Greece, from where the name magnetite derives [1,2]. Modern knowledge on how to tailor these magnetic properties, even at the nanoscale, forms the basis for applications in a wide range of fields such as magnetic resonance imaging, data storage, catalysis and water purification [1,3]. Magnetite nanoparticles are also biodegradable and considered to be non-toxic, making them exceptionally interesting for biomedical applications such as hyperthermia cancer treatment and targeted drug delivery [4].

For most applications of magnetite nanoparticles, excellent control over composition, morphology, size and size distribution must be attained since these particle characteristics dictate the function-determining magnetic properties [5–9]. For example, in hyperthermia cancer therapy, magnetic effects unique to nanosized objects can be fully exploited provided that the saturation magnetization is kept at a maximum. Magnetite nanoparticles smaller than 20–25 nm exhibit superparamagnetism at room temperature, which allows efficient heating of the nanoparticles when an alternating field is applied, while otherwise minimizing interactions between them [10]. This size range is additionally advantageous to benefit from enhanced permeability and retention in tumors, and minimized recognition by the immune system [4]. In terms of shape, non-spherical magnetite particles have demonstrated enhanced hyperthermic heating [9,11].

As small changes in size and morphology can drastically alter the magnetic properties of particles, synthesis methods allowing excellent control are desired. Due to its industrial relevance, diverse synthetic routes for magnetite production have been developed over the last decades. The common goal of these synthetic approaches is to produce magnetite particles with fine-tuned size and shape, and narrow size distribution, using a reproducible process without complex purification procedures. Among the available methods, so far, thermal decomposition of iron-containing organometallic compounds, hydrothermal synthesis and polyol-mediated synthesis have proved superior in meeting the size-related goals [12]. However, these methods require extreme conditions of temperature and pressure, use organic additives or solvents, and in some cases generate toxic byproducts [13]. On the other hand, green synthesis routes employing an aqueous environment, moderate temperatures and nontoxic reagents have not achieved a comparable level of control over magnetite crystallization, especially in terms of producing uniform, size-controlled particles. In addition, the reproducibility of current synthetic methods that are able to manufacture high quality magnetic nanoparticles on a large scale, is still a major challenge [14]. Therefore, establishing generic sustainable routes to synthesize magnetite particles with tailored properties is an appealing task for fundamental scientific interest, and a pressing need for many technological applications.

Efficient particle design from a crystallization reaction requires understanding the underlying formation mechanisms and optimization of thermodynamic and kinetic variables to control nucleation, growth and aggregation/agglomeration stages, accordingly [15]. Supersaturation, the dimensionless driving force for crystallization, is the most important variable to regulate the mechanisms and kinetics of crystallization subprocesses in a precipitation reaction, and can be defined as given in Eq. (1) for magnetite, where *a* represents the activity of each ion forming magnetite, Ksp is the temperature dependent solubility product and v is the total number of moles of ions in one mole of solute. Consumption of supersaturation via the nucleation and growth stages of particle formation and the relative rates of these processes dictate particle size, size distribution and morphology. At the same time, supersaturation is the main regulator of nucleation and growth kinetics [16].

$$S_{magnetite} = \left(\frac{a_{Fe^{3+}}\, a_{Fe^{2+}}\, a_{OH^-}}{K_{sp}} \right)^{1/\nu} \quad (1)$$

The main difficulties for effective control of magnetite synthesis are two-fold. The low solubility of iron oxide minerals results in highly supersaturated, labile solutions so that the task of decoupling nucleation and growth stages for efficient size control becomes formidable. In addition, iron oxide and (oxy)hydroxides can precipitate as several phases that differ in chemical composition and/or lattice structure, which necessitates designated reaction conditions to dictate precipitation of a target phase, and further narrows the parameter window [17]. Multistep formation pathways inspired by biological magnetite formation, e.g. in magnetotactic bacteria, offer green synthesis routes, in which a metastable poorly crystalline phase, such as ferrihydrite or green rust, can be exploited to achieve a better control over the supersaturation profile, and molecular additives aid in directing nucleation and growth of precipitating phases [18–20]. However, despite the demonstrated potential, successful implementations of bioinspired magnetite synthesis leading to size and shape-controlled magnetite have been limited. A recent work by Kuhrts et al. has pioneered application of a bioinspired, multistep crystallization route for tailored magnetite synthesis, and demonstrated the significance of understanding the fundamental crystallization mechanisms to achieve that synthetic capacity [21].

In this work, magnetite nanoparticles were synthesized by the bioinspired coprecipitation of iron(III) chloride and iron(II) sulfate salts. A base solution was slowly titrated into the reaction solution to initiate a multistep precipitation reaction, with the aim to control the crystallization pathway and kinetics via a slow supply of one reactant. Secondly, polyethylene glycol (PEG) and carboxylated PEG (COOH-PEG) were used as additives during the synthesis. Although biomineralization proteins and amino acids have been efficiently used for tailoring particles in similar systems, additives with reduced complexity and cost are preferable, providing that they exert a similar level of efficiency in directing magnetite nucleation and growth [22]. Additionally, PEG is a biocompatible polymer that is often used to coat the final particles for biomedical applications. By varying the experimental conditions of titration rate and additive type and concentration, this study aimed to understand the correlation between particle characteristics and magnetic properties in regards to formation pathways.

2. Materials and methods

2.1. Synthesis of magnetite nanoparticles

Magnetite nanoparticles were synthesized by coprecipitation of iron (III) chloride hexahydrate (Sigma-Aldrich, 97%) and iron(II) sulfate heptahydrate (Sigma-Aldrich, 99.0%) salts with titration of sodium hydroxide (NaOH). All experiments were carried out in a magnetically stirred 350 mL double jacketed glass reactor (supplementary information, section A, Fig. S1). A water bath was used to control the temperature at 25 °C and the magnetic stirrer was kept at 500 rpm. The reactor lid had four inlets and a Metrohm Biotrode pH probe was inserted into one, a titrator tube used for the addition of basic solution was inserted into another and the two last were used as nitrogen gas (N_2) inlet and outlet. The pH probe was controlled by the Tiamo software and recorded the pH continuously during the syntheses. Deionized water flushed with N_2 gas for at least two hours was used for the preparation of all solutions and N_2 gas saturated with water was flushed through the reactor during the entire syntheses to maintain an inert atmosphere in the reaction medium.

For the synthesis, an aqueous solution of iron precursors was prepared in a 200 mL volumetric flask and the total concentration of iron ions was 9 mM. The molar ratio between Fe^{3+} and Fe^{2+} ions was 2:1, corresponding to the stoichiometric ratio in the magnetite structure. In

experiments where polyethylene glycol (PEG, M_n = 4600, Sigma-Aldrich) or O-(2-carboxyethyl) polyethylene glycol (COOH-PEG, M_n = 5000, Sigma-Aldrich) were used as additives during synthesis, an aqueous polymer solution was prepared and filtered with a 0.20 μm syringe filter, diluted to desired concentrations of 1:20, 1:50 and 1:80 additive: total iron concentration and added to the precursor solution. Next, 4.8 mL of 1 M NaOH solution was slowly titrated into the system, controlled by a Metrohm Titrando 902 titrator. A small vial containing sodium hydroxide pellets was attached to the ventilation inlet of the titration burette to prevent carbon dioxide intrusion. The titration rate was set at 0.12 mL min^{-1}, resulting in a 40 min titration time and an increase in relative concentration between hydroxyl ions and total iron concentration, R, by 0.0667 min^{-1} until reaching the stoichiometric value of R = 2.667. Preliminary experiments were performed with varying titration rate and total iron concentrations to determine the experimental values used in this work that induces a multi-step formation mechanism with magnetite as the final product (supplementary information, section B, Table S1). A minimum of two parallels were performed for each experimental condition. After the base titration was completed, the reactions were allowed to proceed for 15 min to ensure completion, as indicated by stabilization of the pH. The reaction solution was then divided into four Eppendorf tubes and the precipitate was collected via magnetic decantation and washed two times with 25 mL nitrogen flushed DI water. In some experiments, the particles were subsequently coated with PEG. This was done by adding 5 mL of a 50 wt/v % PEG solution to each Eppendorf tube. Peptization was done by ultrasonication for 2 min and the particles were collected by centrifuging at 4000 rpm. An additional washing step with nitrogen flushed DI water was followed to remove excess PEG. The final products were dried overnight in a vacuum desiccator and stored at 4 °C.

2.2. Micro-Raman spectroscopy

μ-Raman spectroscopy was performed using a Renishaw InVia Reflex Spectrometer System for Raman spectral analysis with a 100 mW 532 nm VIS excitation laser. It was equipped with a thermoelectrically cooled CCD detector and 2400 grooves/mm diffraction grating. The instrument was controlled by Renishaw's WiRE software and the software's option to filter cosmic rays based on extra background accumulations was applied. For the analysis, 0.1% laser power, 30-s exposure time and 4 accumulations were used through a 100× lens. The analysis conditions were optimized to achieve a high signal-to-noise ratio without inducing the oxidation of magnetite samples into maghemite or hematite. Details of the optimization studies are given in supplementary information, section C (Fig. S2). Samples were prepared by taking 1 mL aliquots of the solution from the reactor at determined time points, collecting the solid precipitate via centrifugation and distributing them onto a small area of a microscope slide.

2.3. X-ray powder diffraction

For X-ray powder diffraction (XRD), a Bruker AXS GmbH D8 Focus powder diffraction system with Cu K-α radiation was used. Dried powder samples were scanned for 2θ ranging from 10° to 80° using a 1.0 mm slit. The spectra were obtained with 0.0243 step size and 0.8 s measurement time at each step. Analyses of the obtained diffraction patterns and calculations of quantitative information were performed in the Bruker Topas software. The Pawley method with the fundamental parameters approach was used for estimating the lattice parameters and crystallite sizes. The background was approximated by 7th order Chebyshev polynomials. The details of Pawley fitting and the fitted spectra are given in supplementary information, section D (Fig. S3).

2.4. Vibrational sample magnetometer

Magnetic hysteresis loops were measured using a PMC MicroMag 3900 Series vibrating sample magnetometer (VSM) at room temperature. Maximal field strength was 1 T, with a step size of 0.01 T and averaging time at each step was 0.2 s. The vibrating frequency was 83 Hz. Paramagnetic and diamagnetic contributions from the background and sample holder were compensated for by slope corrections based on the assumption that the curve should be flat above 0.75 T. Dried samples were used, and 13 ± 0.5 mg of dried powder was added to a gelatin capsule which served as sample holder. The Langevin function was fitted using non-linear least-squares. The detailed description of Langevin fitting is given in supplementary information, section E (Fig. S4).

2.5. Transmission electron microscopy

Transmission electron microscopy (TEM) was performed using a JEOL JEM 2100 microscope fitted with a LaB6 cathode at an accelerating voltage of 200 kV. Samples were prepared by drop-casting 3 μL of solutions directly from the reaction media onto carbon-coated 300 mesh copper grids at determined time points. Average particle diameter and standard deviation were calculated by counting 350–500 particles per sample by using ImageJ. Diffraction patterns were analyzed using DiffTools in Digital Micrograph software (version 2.32, Gatan).

2.6. Thermal analyses

Thermogravimetric analysis (TGA) was performed using a NETZSCH TG 209F1 Libra thermal analyzer. For TGA, dry powder samples were heated from room temperature to 650 °C with a temperature ramp of 10 °C min^{-1} under a nitrogen atmosphere with a flow rate of 40 mL min^{-1}.

3. Results

3.1. Magnetite formation pathway

The formation pathway of magnetite nanoparticles was followed by in-situ measurements of solution pH during the reaction and ex-situ characterization of solid precipitates at predetermined time points. In all experiments, despite the continuous addition of a strong base, the pH remained nearly constant until approximately 3 mL of the base solution was added, corresponding to R = 1.667 (Fig. 1a). This remarked the nucleation and growth of a first precipitate, involving rapid consumption of hydroxide ions. Observations on the pH profile were accompanied by visual changes in solution turbidity and color, verifying precipitation (Fig. S5). Subsequently, the pH increased abruptly, indicating that the added base was no longer entirely consumed by precipitation. However, the curves quickly flattened and formed a second plateau with a moderate pH increase. This indicated the emergence of a new phase with a different stoichiometry. After this step, another period with a rapid increase in pH was observed. When all the base solution was added, the pH increase terminated immediately. Analyses of samples collected at the end of experiments by μ-Raman and XRD verified magnetite as the final product (Fig. 1 b,c). When PEG or COOH-PEG were used as additives at different concentrations, the typical shape of the pH curves remained similar, indicating no fundamental changes in the crystallization pathway. However, the second plateau appeared at higher pH values, demonstrating that formation of the second phase, leading to magnetite, was delayed, an effect previously observed when polypeptides were used as additives in coprecipitation reactions [23].

The multi-step crystallization pathway indicated by the pH curves has previously been documented, and the titration rate of the base was shown to dictate the reaction progression and emergence of different iron (hydr)oxide phases [1,18,19,24]. To associate the evolution of the pH curves with the progression of the precipitation reaction, samples were collected during the first and second plateaus of the additive-free synthesis (Fig. 2a-c). During the formation of magnetite, either synthetically via coprecipitation or biologically in magnetotactic bacteria,

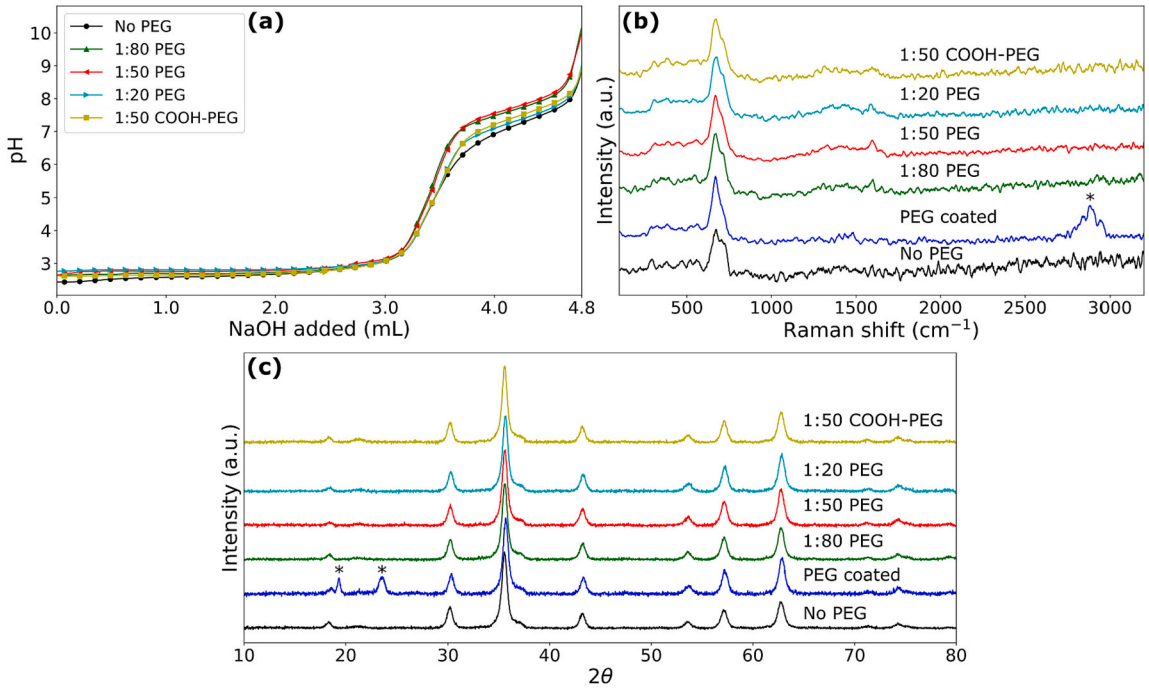

Fig. 1. (a) Evolution of pH in the reaction medium as a function of base titration, (b) μ-Raman and (c) XRD spectra of final products from synthesis with and without additives, with peaks corresponding to PEG marked with an asterisk.

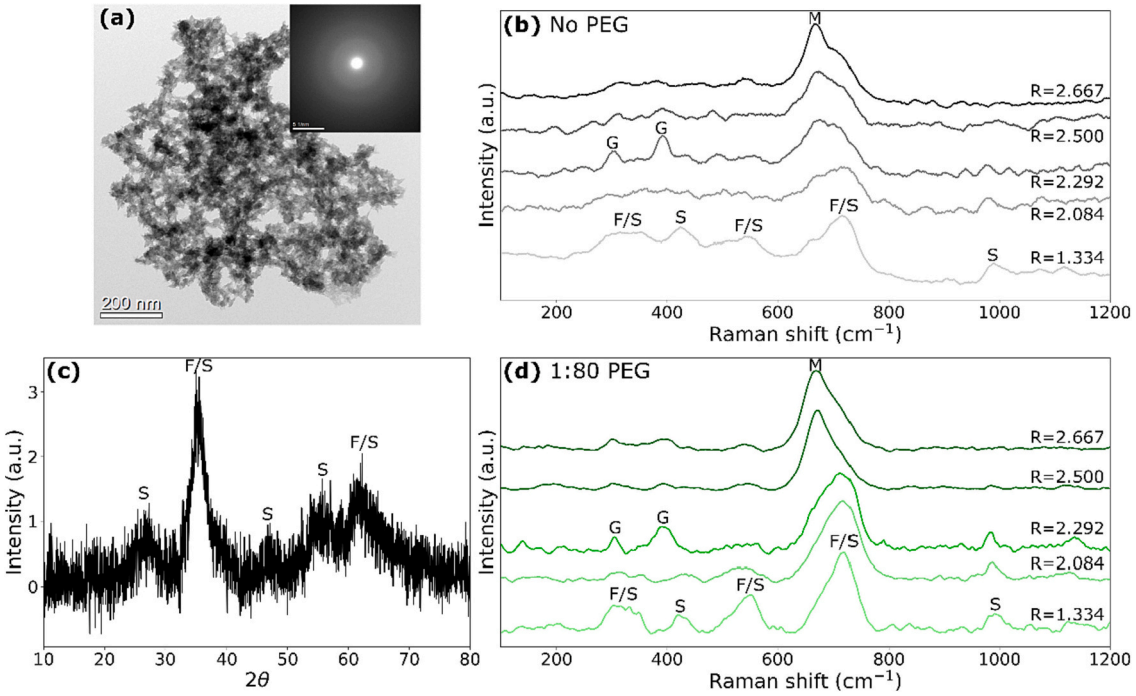

Fig. 2. (a) TEM image and corresponding SAED pattern (inset) of the precipitate collected at the first plateau at $R = 1.334$, (b) time-resolved Raman spectra of samples collected at indicated R values, and (c) XRD spectrum of the precipitate collected at the first plateau during the additive-free reaction, (d) time-resolved Raman spectra of samples collected at indicated R values in the presence of 1:80 PEG concentration. The peaks corresponding to different phases are marked with (F) for ferrihydrite, (G) for goethite, (S) for schwertmannite, and (M) for magnetite.

amorphous ferrihydrite has been suggested to form as a precursor phase [1,25]. TEM images and the corresponding SAED pattern displayed the amorphous nature of the precipitate collected during the first plateau (Fig. 2a). The Raman spectrum corresponding to ferrihydrite varies slightly depending on its exact structure, however, it typically produces a characteristic strong peak at 710 cm^{-1}, medium peaks at 550 cm^{-1} and 350 cm^{-1} and a broad weak peak at 1380–1400 cm^{-1} [26,27]. This corresponded well with the observed spectra (Fig. 2b). On the other hand, the peaks at just above 400 cm^{-1} and below 1000 cm^{-1} are not typically observed for ferrihydrite but could correspond to akaganeite or schwertmannite [28,29]. Due to otherwise partly overlapping peaks, these phases might be difficult to distinguish from ferrihydrite. XRD

spectrum of the sample collected at the first plateau showed broad, poorly-defined peaks that could correspond to both ferrihydrite and schwertmannite, while excluding akaganeite (Fig. 2c) [30].

After the first plateau, the pH increased abruptly. Increasing pH in the reaction medium changes the stability of different iron (hydr)oxides, and the reactivity of ferrous ions increases dramatically [31,32]. Consequently, the emergence of new phases and transformation of metastable phases are induced, involving the consumption of hydroxide ions as indicated by the formation of a second plateau in the pH curves. To track the reaction progression, additional intermediate samples were taken at the beginning, middle, and end of the second plateau for μ-Raman analyses (Fig. 2b). The precipitate collected at the very beginning of the second plateau ($R = 2.084$), where the pH was between 6 and 7, displayed the characteristic ferrihydrite peak at 710 cm^{-1}. Additionally, a shoulder at 670 cm^{-1} was observed, indicating that some magnetite had already been formed. When 4.125 mL of the base was added, corresponding to $R = 2.292$, the characteristic magnetite peak was more intense than the ferrihydrite peak, demonstrating that magnetite formed at the expense of ferrihydrite. Furthermore, the presence of weak peaks at 390 cm^{-1} and 300 cm^{-1} indicated small amounts of goethite. At the end of the plateau ($R = 2.500$), magnetite was the dominating product and the goethite peaks were almost completely lost, showing goethite to be a transient phase with a short lifetime in solution. Preliminary experiments showed that the goethite intermediate had a longer lifetime in solution and a significant presence in the final product when the base titration rate was reduced to one-third (Table S1).

In order to elucidate the effects of PEG additives on the reaction pathway, time-resolved Raman analyses were conducted on samples collected during a reaction with 1:80 PEG concentration (Fig. 2d). Similar to the additive-free synthesis, the sample collected at the first plateau ($R = 1.334$) showed ferrihydrite associated peaks. The reaction pathway followed with limited appearance of goethite ($R = 2.292$) and magnetite formation during the second plateau, yet with a delay in its formation. In contrast to the additive-free case, the magnetite associated peaks were not manifested before the end of the second plateau was reached ($R = 2.500$).

3.2. Particle properties

3.2.1. Magnetic properties

Magnetization curves of particles synthesized with and without additives, and with PEG coating are given in Fig. 3. The very low remanence and coercivity as well as close-fitting of experimental data with the Langevin function confirmed superparamagnetic behavior for all samples [33]. The slight deviation from zero remanence and coercivity can be explained by the presence of particles above 20 to 25 nm that are sufficiently large to be thermally blocked at room temperature. The estimated values for M_S, M_R and B_c are given in Table 1.

The measured saturation magnetization for particles from additive-free synthesis, 57.2 $Am^2\ kg^{-1}$ was within expectations for pure magnetite nanoparticles in the superparamagnetic size range [6,23,34]. When PEG or COOH-PEG were used as additives during the synthesis, saturation magnetization, relative remanence and coercivity was higher for all samples. The change in magnitude showed an inverse relation to the additive concentration for PEG and the presence of COOH-PEG resulted in a lower increase. Here, it is important to note that saturation magnetization is normalized by volume or weight and is determined by the material, independent of size for a bulk sample. Since the magnetization of magnetite is a result of its crystalline structure, it may be decreased by e.g., presence of defects or impurities. Additionally, for nanoparticles, the magnetic dead layer on and close to the surface becomes significant, resulting in size-dependent saturation magnetization [5,35]. Consequently, it is more precise to view the effect of the PEG additives as limiting the decrease in magnetization, rather than resulting in an increase. In order to put the magnitude of the magnetization changes in context, the size-dependent magnetization values of magnetite nanoparticles reported by Li et al. are used. Li et al. reported that the magnetization increased by 11%, from 54.7 to 60.9 $Am^2\ kg^{-1}$, when magnetite particle size was increased from 9.6 to 19.6 nm [6]. In this work, the magnetization was increased by up to 15% in the presence of PEG additives, demonstrating a significant effect. Conversely, particles coated with PEG post-synthesis showed reduced saturation magnetization, lower remanence and coercivity compared to particles from additive-free synthesis due to the non-magnetic dead weight of PEG, where its presence is confirmed by μ-Raman, XRD, and TGA spectra

Table 1
The saturation magnetization (M_S), remanent magnetization (M_R), coercivity (B_c), and magnetic moment (μ) per particle obtained by the VSM results and the Langevin fit.

	M_S ($Am^2\ kg^{-1}$)	M_R ($Am^2\ kg^{-1}$)	B_c (mT)	μ (10^{-19} Am^2)
no PEG	57.20	1.20	0.59	3.3
w/ 1:80 PEG	65.80	2.20	1.13	2.9
w/ 1:50 PEG	64.30	2.50	1.29	2.9
w/ 1:20 PEG	63.20	2.10	1.13	2.8
w/ 1:50 COOH-PEG	60.50	2.50	1.28	2.9
w/ PEG coating	47.80	0.70	0.46	3.4

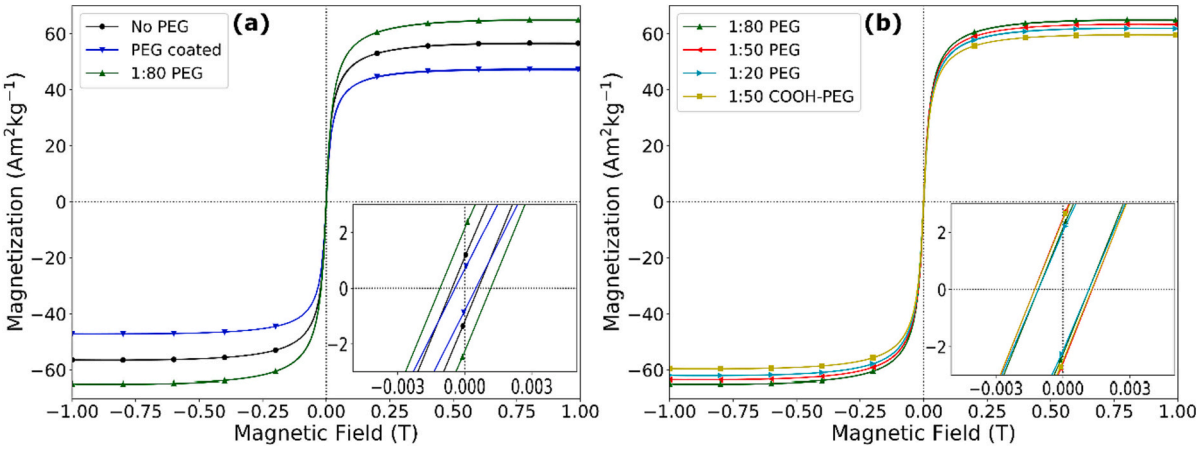

Fig. 3. Magnetization curves obtained by VSM analysis at room temperature of dried particles synthesized at indicated experimental conditions; (a) shows magnetization curves obtained for bare particles, and particles with highest and lowest magnetization values for easy comparison, (b) shows concentration dependence of magnetization of particles precipitated with additives.

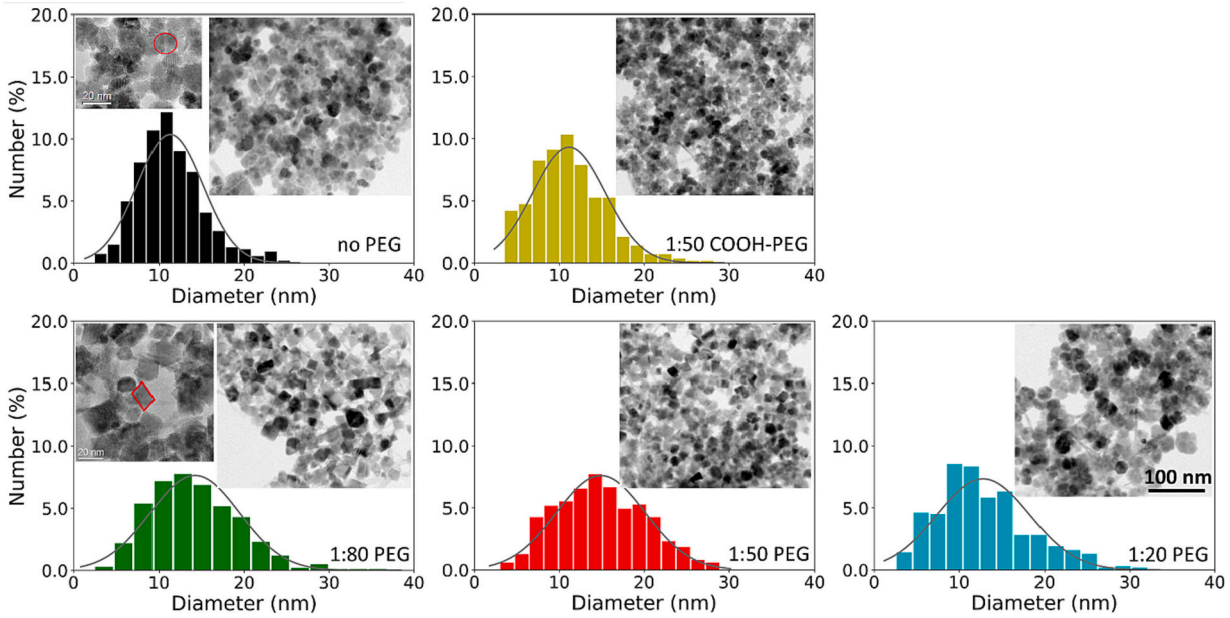

Fig. 4. TEM images and the corresponding size distribution of final particles precipitated at the indicated experimental conditions. High resolution images are given as insets for "no PEG" and "1:80 PEG" conditions to display the typical particle morphologies.

(Fig. 1 and Fig. S6) [34,36].

3.2.2. Composition, size and morphology

The particle characteristics of the final precipitates were investigated to explain the enhanced magnetic properties of magnetite nanoparticles synthesized in the presence of PEG additives. As previously mentioned, all experiments regardless of additive presence resulted in magnetite formation as confirmed by XRD and μ-Raman analyses, and no significant variations in phase composition were observed between experimental sets (Fig. 1).

TEM images were used to determine the particle size and size distribution of magnetite nanoparticles and to investigate their morphology (Fig. 4). The data showed some variation in particle size with additive presence, where the size distributions were broader and shifted towards larger particles for the samples synthesized with additives. This was also reflected in the percentage of particles above 22.0 nm, an approximate limit for superparamagnetism at room temperature for magnetite nanoparticles (Table 2), which is typically between 20 and 25 nm [1,10], and correlating with the increased coercivity and remanent magnetization. Thus, the shift in particle size to higher values was evaluated as a possible reason for the increased saturation magnetization. However, the differences in particle size were small and within the standard deviations. In addition, when COOH-PEG was used as an additive, neither particle size nor the percentage of particles above 22.0 nm was increased. Nonetheless, the remanence, coercivity and saturation magnetization were higher compared to additive-free synthesis, indicating that the particle size alone was not sufficient to explain the magnetic results.

Pawley fitting of the XRD spectra of final samples showed values close to 1.0 for the goodness of fit (GOF) and estimated lattice parameters close to the expected for magnetite, 8.39 Å, which indicated highly crystalline particles (Table 2 and Table S2) [1]. The crystallite sizes estimated by the Pawley method showed higher values for particles synthesized with additives and correlated with increasing saturation magnetization. Since it is only the crystalline part of a particle that will contribute to the magnetic response, a significantly decreased dead layer thickness can result in larger crystallite size, despite the solid particle size being unchanged, and result in higher saturation magnetization. TEM images also reflected subtle differences in morphology, where faceted particles were observed more commonly in the presence of additives. In addition to the improved crystallinity, faceting of magnetite nanoparticles in the presence of PEG additives can also result in smaller particles being ferrimagnetic at room temperature and consequently have increased remanence and coercivity due to increasing magnetostatic anisotropy energy [6].

The magnetic sizes were estimated based on the fitting of the Langevin function and summarized in Table 2. In contrast to crystallite and TEM sizes, a slight decrease is observed in the presence of PEG additives. However, the fundamental assumption of Langevin fitting is that the particles are superparamagnetic. The size estimation is based on how fast the magnetization is increased, i.e., the alignment of magnetic moments, which determines the shape of the curve [5]. The magnetic moments in particles above the superparamagnetic size are blocked, and consequently require a stronger applied field to align with it. This deviation from superparamagnetic behavior results in smaller estimated particle sizes despite the particles being larger. Consequently, the

Table 2
Average particle diameter, d_{part} (nm), and crystallite size of particle populations obtained by different characterization methods.

	TEM size d_{part} (nm)	TEM size d_{part} > 22 nm (%)	Pawley fit crystallite size (nm)	Langevin fit d_{part} (nm)
no additive	11.3 ± 3.9	1.7	9.6	11.0
w/ 1:80 PEG	14.2 ± 5.2	7.1	10.4	10.5
w/ 1:50 PEG	14.9 ± 5.2	9.6	10.1	10.5
w/ 1:20 PEG	12.8 ± 5.4	7.3	10.1	10.4
w/ 1:50 COOH-PEG	11.2 ± 4.3	1.2	10.4	10.5

increased amount of ferrimagnetic particles observed by TEM for the particles synthesized in the presence of PEG additives explains the trend.

4. Discussion

Our results demonstrated that the PEG additives affected particle size and size distribution, crystallinity, and morphology of the magnetite nanoparticles, which were reflected in their magnetic properties. Since the listed particle characteristics are determined during the nucleation and growth stages of particle formation, the regulatory roles of PEG additives on these steps must be understood to advance our synthetic design capabilities.

The pH curves demonstrated a two-step formation pathway, and characterization of the precipitation products displayed initial formation of ferrihydrite (Eq. (2)) followed by precipitation of magnetite (Eq. (3)) in correlation with two plateaus corresponding to significant base consumption (Fig. 5). Although the shape of pH curves was similar in all experiments, the second plateau was observed at higher pH values in the presence of additives. The shift in pH was observed in the wake of a delay in the formation of magnetite. Similar results were previously reported by Lenders et al. when polypeptides were used as additives in bioinspired coprecipitation and explained by retardation of magnetite nucleation due to stabilization of ferrihydrite and reduced activity of ferrous ions [23]. However, nucleation of magnetite at higher pH typically resulted in smaller particles and correspondingly decreased magnetization, in contrast to our results [37,38]. The decrease in size was attributed to higher nucleation rates evoked by the increased supersaturation with respect to magnetite at the nucleation stage, and a decrease in surface tension with increasing surface charge density at higher pH [23,39].

$$Fe^{3+}(aq) + 3\ OH^{-}(aq) \rightarrow Fe(OH)_3\ (s) \quad (2)$$

$$2\ Fe(OH)_3(s) + Fe^{2+}(aq) + 2\ OH^{-}(aq) \rightarrow Fe_3O_4\ (s) + 4H_2O \quad (3)$$

On the other hand, depending on the exact synthesis routes, type of additives, and their concentration, the presence of additives was reported to result in improved crystallinity with reduced defects and larger, more faceted particles similar to our results [13,40–42]. Such outcomes were consistently observed in systems with multistep crystallization pathways, where the additives stabilized the intermediate phases either via ionotropic effects, complexation, selective adsorption, steric hindrance or templating [43–45]. Our results clearly exhibited a multistep crystallization pathway, in which the intermediate ferrihydrite phase was stabilized by the presence of PEG, delaying magnetite formation. There is consensus in the literature that magnetite emerges via heterogeneous nucleation in multistep pathways, using the precursor amorphous phase as a substrate [15,36]. From a classical crystallization point of view, stabilization of the precursor phase, i.e., increase of its lifetime, results from the delay in the formation of more stable phases, which thermodynamically drives the phase transformation. Additives can impede crystallization kinetics by (i) sequestering free ions in the solution, (ii) limiting the availability of the precursor surface for heterogeneous nucleation of the stable phases, and (iii) affecting the dissolution rate of the precursor phase. Eq. (3) shows the significance of ferrous ions in magnetite formation via ferrihydrite transformation. Therefore, we investigated possible complexation between PEG additives and ferrous ions via spectroscopic methods (supplementary information, section H). Analyses via both Fourier transform infrared (FTIR) spectroscopy and UV–vis spectroscopy indicated little interaction between PEG and iron ions in solution (Fig. S7). As a result, we eliminated ion complexation as a possible cause of delay for magnetite formation.

The supersaturation profile during the phase transformation is determined both by the formation rate of crystalline phase, i.e. magnetite, and the dissolution rate of ferrihydrite [46]. Stabilization of the ferrihydrite by PEG additives may result from reduced accessibility of the ferrihydrite surface for heterogeneous magnetite nucleation. This, together with slow release of magnetite forming ions via ferrihydrite dissolution that is induced by phase transformation, maintains the supersaturation in the reaction medium [47]. The resulting supersaturation profile favors magnetite growth, rather than uncontrolled nucleation events, leading to increased particle size; and slow growth kinetics and growth mechanisms leading to faceting [48,49]. Similar results on magnetite nanoparticles have been reported when lysine, an amino acid, was used as an additive, attributed to stabilization and slow dissolution of initially formed nuclei or particles [13].

XRD and μ-Raman characterization of final particles did not show PEG presence, and both TGA analysis (Fig. S6) and zeta potential measurements (Fig. S8) showed similar results for magnetite particles formed with and without PEG additives. This indicated that the additive molecules were not adsorbed on or incorporated into the magnetite particles, but were mainly associated with the precursor phase. The achieved increase in saturation magnetization by PEG additive is therefore attributed to the stabilization of the ferrihydrite precursor phase, resulting in a controlled level of supersaturation and

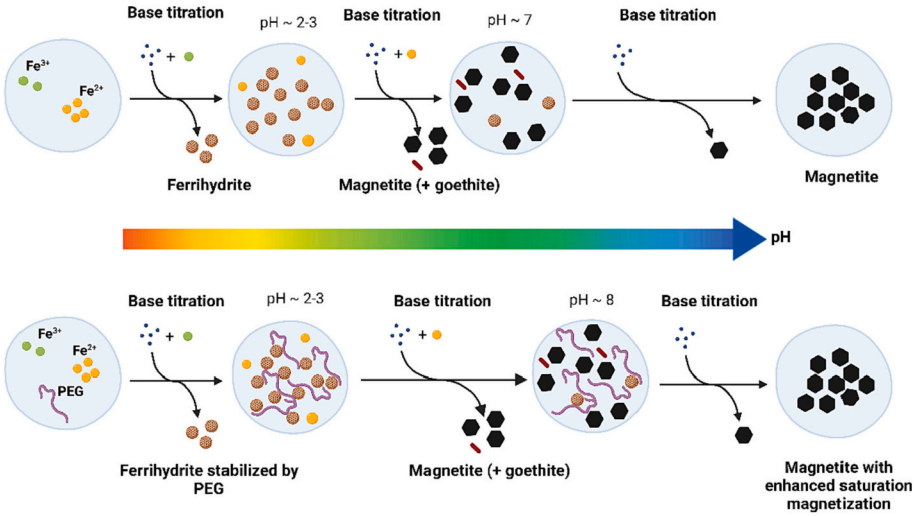

Fig. 5. Schematic representation of the multistep reaction pathway for magnetite formation (black hexagons) via ferrihydrite intermediate (brown spheres) and short-lived goethite (red needles) in the absence and presence of PEG additive (purple strings). (For interpretation of the references to color in this figure legend, the reader is referred to the web version of this article.)

consequently larger, faceted particles. At the same time, PEG did not stabilize the ferrihydrite to an extent, where nucleation of magnetite is delayed to significantly higher pH resulting in smaller particles [23,37], or inhibited completely [13,50].

The regulating effects of protein or amino acid additives on magnetite formation have been mostly attributed to their size, charge and hydrophobicity [23]. The PEG additives used in this work are at comparable molecular weight and both hydrophilic, yet differ in their functional groups. The PEG additive carries no net charge, whereas COOH-PEG contains a carboxyl group with a pKa value of 4–5 (Fig. S9). When the particles synthesized in the presence of PEG and COOH-PEG at equal concentration are compared, it becomes evident that the stabilization of ferrihydrite was not driven by the ionotropic effects of the additive. Here, it should be noted that in the pH range of ferrihydrite formation (pH ~ 2–3), both additives would have a neutral charge. Yet, COOH-PEG would bear a negatively charged carboxyl group in the pH zone where phase transformation is initiated. Thus, surface adsorption, steric hindrance or templating should be considered to explain the stabilization of the intermediate phase and delayed magnetite formation [42]. As shown in Table 1, the saturation magnetization of particles showed an inverse relationship with the PEG concentration, however, neither the particle size nor the faceting could explain this behavior alone. A possible explanation could be stabilization of small amounts of non-magnetic goethite in the presence of additives in a concentration-dependent manner. The preliminary experiments with slower base titration showed that the goethite content increases when the pH in the reaction medium was below 7 for longer periods of time (Table S1). The phase transformation of both ferrihydrite and goethite to magnetite is known to be catalyzed by ferrous ions and is initiated around pH 7 with a rate increasing with increasing pH [51,52]. Although the presence of goethite was not detected in final samples by the XRD and μ-Raman analysis, TEM images showed presence of needle-like particles, a typical morphology for goethite (Fig. S10) [44]. Thus, it is proposed that goethite content in the final precipitate could be increased with additive concentration via its stabilization, leading to a decrease in saturation magnetization, together with variations in particle size distribution and morphology. This would also explain why the COOH-PEG, which stabilizes goethite more efficiently than PEG due to its ionic nature at pH above 5, enhanced the saturation magnetization to a lesser extent. Due to falling below the detection limit of XRD and μ-Raman analyses, quantitative determination of goethite amount was not possible.

5. Conclusion

Bioinspired coprecipitation method offers a versatile synthesis platform for magnetite nanoparticles. Yet, in order to fully exploit the potential for production of tailored particles via this green method, the correlation between the particle characteristics and the formation pathway should be established.

Our results showed that properties of magnetite nanoparticles can be manipulated by the use of PEG additives during the multistep precipitation pathway, resulting in enhanced saturation magnetization. PEG additives were chosen due to their biocompatibility and to examine the interaction mode of these low-complexity molecules with the precipitating phases. The effects of additives on the particle characteristics were associated with their ability to stabilize the intermediate iron hydroxide phases, and affect the kinetics of phase transformation reactions. We have shown that ionotropic effects were not the dominating contributor to the stabilization, however, additional experiments with a wider range of PEG concentration and varying chain lengths are needed to explore the structural characteristics of PEG additives responsible for directing magnetite formation.

The high complexity of iron (hydr)oxide precipitation system makes it notoriously difficult to fine-tune final products in solution synthesis, where precipitation of multiple phases and phase transformations are probable. However, with the insight provided by systematic studies on crystallization pathways and kinetics, bioinspired multistep precipitation methods can be implemented with greater control and offer green alternatives for production of tailored magnetite nanoparticles.

CRediT authorship contribution statement

Andreas Bogen Kristiansen: Conceptualization, Methodology, Formal analysis, Investigation, Visualization, Writing – original draft, Writing – review & editing. **Nathan Church:** Formal analysis, Writing – review & editing. **Seniz Ucar:** Conceptualization, Methodology, Writing – original draft, Writing – review & editing, Supervision, Project administration.

Declaration of Competing Interest

The authors declare that they have no known competing financial interests or personal relationships that could have appeared to influence the work reported in this paper.

Data availability

Data will be made available on request.

Acknowledgements

The Research Council of Norway is acknowledged for the support to the Norwegian Micro and Nanofabrication Facility, NorFab (project number 295864), and the Norwegian Center for Transmission Electron Microscopy, NORTEM (project number 197405/F50). We thank Karthik Raghunathan for his assistance with the UV–vis spectroscopy measurements. Fig. 5 is created with Biorender.com.

Appendix A. Supplementary data

Supplementary data to this article can be found online at https://doi.org/10.1016/j.powtec.2022.118145.

References

[1] G. Mirabello, J.J.M. Lenders, N.A.J.M. Sommerdijk, Bioinspired synthesis of magnetite nanoparticles, Chem. Soc. Rev. 45 (2016) 5085–5106, https://doi.org/10.1039/C6CS00432F.
[2] V. Melfos, B. Helly, P. Voudouris, The ancient Greek names “magnesia” and “Magnetes” and their origin from the magnetite occurrences at the Mavrovouni mountain of Thessaly, Central Greece. A mineralogical-geochemical approach, Archaeol. Anthropol. Sci. 3 (2011) 165–172, https://doi.org/10.1007/s12520-010-0048-6.
[3] I. Ali, C. Peng, I. Naz, M. Amjed, Chapter 6 - water purification using magnetic nanomaterials: an overview, in: Magnetic Nanostructures, Springer Nature Switzerland AG, 2019.
[4] R.A. Revia, M. Zhang, Magnetite nanoparticles for cancer diagnosis, treatment, and treatment monitoring: recent advances, Mater. Today 19 (2016) 157–168, https://doi.org/10.1016/j.mattod.2015.08.022.
[5] D.-X. Chen, A. Sanchez, E. Taboada, A. Roig, N. Sun, H.-C. Gu, Size determination of superparamagnetic nanoparticles from magnetization curve, J. Appl. Phys. 105 (2009) 83924, https://doi.org/10.1063/1.3117512.
[6] Q. Li, C.W. Kartikowati, S. Horie, T. Ogi, T. Iwaki, K. Okuyama, Correlation between particle size/domain structure and magnetic properties of highly crystalline Fe3O4 nanoparticles, Sci. Rep. 7 (2017) 9894, https://doi.org/10.1038/s41598-017-09897-5.
[7] M. Unni, A.M. Uhl, S. Savliwala, B.H. Savitzky, R. Dhavalikar, N. Garraud, D. P. Arnold, L.F. Kourkoutis, J.S. Andrew, C. Rinaldi, Thermal decomposition synthesis of iron oxide nanoparticles with diminished magnetic dead layer by controlled addition of oxygen, ACS Nano 11 (2017) 2284–2303, https://doi.org/10.1021/acsnano.7b00609.
[8] A.G. Roca, D. Niznansky, J. Poltierova-Vejpravova, B. Bittova, M.A. González-Fernández, C.J. Serna, M.P. Morales, Magnetite nanoparticles with no surface spin canting, J. Appl. Phys. 105 (2009), 114309, https://doi.org/10.1063/1.3133228.
[9] R. Moreno, S. Poyser, D. Meilak, A. Meo, S. Jenkins, V.K. Lazarov, G. Vallejo-Fernandez, S. Majetich, R.F.L. Evans, The role of faceting and elongation on the magnetic anisotropy of magnetite Fe3O4 nanocrystals, Sci. Rep. 10 (2020) 2722, https://doi.org/10.1038/s41598-020-58976-7.
[10] V. Reichel, A. Kovacs, M. Kumari, E. Bereczk-Tompa, E. Schneck, P. Diehle, M. Posfai, A.M. Hirt, M. Duchamp, R.E. Dunin-Borkowski, D. Faivre, Single

crystalline superstructured stable single domain magnetite nanoparticles, Sci. Rep. 7 (2017) 45484, https://doi.org/10.1038/srep45484.
[11] S.K. Shaw, A. Biswas, A. Gangwar, P. Maiti, C.L. Prajapat, S.S. Meena, N.K. Prasad, Synthesis of exchange coupled nanoflowers for efficient magnetic hyperthermia, J. Magn. Magn. Mater. 484 (2019) 437–444, https://doi.org/10.1016/j.jmmm.2019.04.056.
[12] R.K. Sharma, S. Dutta, S. Sharma, R. Zboril, R.S. Varma, M.B. Gawande, Fe3O4 (iron oxide)-supported nanocatalysts: synthesis, characterization and applications in coupling reactions, Green Chem. 18 (2016) 3184–3209, https://doi.org/10.1039/C6GC00864J.
[13] R. Contreras-Montoya, Y. Jabalera, V. Blanco, J.M. Cuerva, C. Jimenez-Lopez, L. Alvarez de Cienfuegos, Lysine as size-control additive in a bioinspired synthesis of pure superparamagnetic magnetite nanoparticles, Cryst. Growth Des. 20 (2020) 533–542, https://doi.org/10.1021/acs.cgd.9b00169.
[14] M.E.F.B. Helena Gavilán, Lucía Gutiérrez, Sabino Veintemillas-Verdaguer, María del Puerto Morales, Controlling the size and shape of uniform magnetic iron oxide nanoparticles for biomedical applications, in: N.T.K. Thanh (Ed.), Clinical Applications of Magnetic Nanoparticles, Taylor and Francis, Boca Raton, 2018.
[15] A.P. Freitas, R.K. Ramamoorthy, M. Durelle, E. Larquet, I. Maurin, F. Testard, C. Chevallard, T. Gacoin, D. Carriere, Crystallization within intermediate amorphous phases determines the polycrystallinity of nanoparticles from coprecipitation, Nano Lett. 22 (2022) 29–35, https://doi.org/10.1021/acs.nanolett.1c02859.
[16] N.T.K. Thanh, N. Maclean, S. Mahiddine, Mechanisms of nucleation and growth of nanoparticles in solution, Chem. Rev. 114 (2014) 7610–7630, https://doi.org/10.1021/cr400544s.
[17] R.M. Cornell, U. Schwertmann, The Iron Oxides: Structure, Properties, Reactions, Occurrences and Uses, Wiley, 2003.
[18] J.J.M. Lenders, C.L. Altan, P.H.H. Bomans, A. Arakaki, S. Bucak, G. de With, N.A.J.M. Sommerdijk, A bioinspired coprecipitation method for the controlled synthesis of magnetite nanoparticles, Cryst. Growth Des. 14 (2014) 5561–5568, https://doi.org/10.1021/cg500816z.
[19] J. Baumgartner, A. Dey, P.H.H. Bomans, C. Le Coadou, P. Fratzl, N.A.J.M. Sommerdijk, D. Faivre, Nucleation and growth of magnetite from solution, Nat. Mater. 12 (2013) 310–314, https://doi.org/10.1038/nmat3558.
[20] T. Prozorov, D.A. Bazylinski, S.K. Mallapragada, R. Prozorov, Novel magnetic nanomaterials inspired by magnetotactic bacteria: topical review, Mater. Sci. Eng. R 74 (2013) 133–172, https://doi.org/10.1016/j.mser.2013.04.002.
[21] L. Kuhrts, S. Prévost, D.M. Chevrier, P. Pekker, O. Spaeker, M. Egglseder, J. Baumgartner, M. Pósfai, D. Faivre, Wettability of magnetite nanoparticles guides growth from stabilized amorphous ferrihydrite, J. Am. Chem. Soc. 143 (2021) 10963–10969, https://doi.org/10.1021/jacs.1c02687.
[22] H. Nudelman, Y.-Z. Lee, Y.-L. Hung, S. Kolusheva, A. Upcher, Y.-C. Chen, J.-Y. Chen, S.-C. Sue, R. Zarivach, Understanding the biomineralization role of magnetite-interacting components (MICs) from Magnetotactic Bacteria, Front. Microbiol. 9 (2018) 2480, https://doi.org/10.3389/fmicb.2018.02480.
[23] J.J.M. Lenders, H.R. Zope, A. Yamagishi, P.H.H. Bomans, A. Arakaki, A. Kros, G. de With, N.A.J.M. Sommerdijk, Bioinspired magnetite crystallization directed by random copolypeptides, Adv. Funct. Mater. 25 (2015) 711–719, https://doi.org/10.1002/adfm.201403585.
[24] T. Ahn, J.H. Kim, H.-M. Yang, J.W. Lee, J.-D. Kim, Formation pathways of magnetite nanoparticles by coprecipitation method, J. Phys. Chem. C 116 (2012) 6069–6076, https://doi.org/10.1021/jp211843g.
[25] M.I. Siponen, P. Legrand, M. Widdrat, S.R. Jones, W.-J. Zhang, M.C.Y. Chang, D. Faivre, P. Arnoux, D. Pignol, Structural insight into magnetochrome-mediated magnetite biomineralization, Nature 502 (2013) 681–684, https://doi.org/10.1038/nature12573.
[26] M. Hanesch, Raman spectroscopy of iron oxides and (oxy)hydroxides at low laser power and possible applications in environmental magnetic studies, Geophys. J. Int. 177 (2009) 941–948, https://doi.org/10.1111/j.1365-246X.2009.04122.x.
[27] A. Dzieniszewska, J. Kyzioł-Komosińska, M. Pajak, Adsorption and bonding strength of chromium species by ferrihydrite from acidic aqueous solutions, PeerJ 8 (2020), e9324, https://doi.org/10.7717/peerj.9324.
[28] L. Mazzetti, P.J. Thistlethwaite, Raman spectra and thermal transformations of ferrihydrite and schwertmannite, J. Raman Spectrosc. 33 (2002) 104–111, https://doi.org/10.1002/jrs.830.
[29] S. Cambier, D. Verreault, G. Frankel, Raman investigation of anodic undermining of coated steel during environmental exposure, Corrosion 70 (2014) 1219–1229, https://doi.org/10.5006/1358.
[30] J.-Y. Yu, B. Heo, I.-K. Choi, J.-P. Cho, H.-W. Chang, Apparent solubilities of schwertmannite and ferrihydrite in natural stream waters polluted by mine drainage, Geochim. Cosmochim. Acta 63 (1999) 3407–3416, https://doi.org/10.1016/S0016-7037(99)00261-6.
[31] Synthesis Pathways, Iron Oxides in the Laboratory, 2000, pp. 55–65.
[32] J.-P. Jolivet, C. Chanéac, E. Tronc, Iron oxide chemistry. From molecular clusters to extended solid networks, Chem. Commun. 5 (2004) 481–483, https://doi.org/10.1039/B304532N.
[33] C. Binns, Chapter 1 - Tutorial section on nanomagnetism, in: C. Binns (Ed.), Frontiers of Nanoscience, Elsevier, 2014, pp. 1–32.
[34] X.L. Liu, H.M. Fan, J.B. Yi, Y. Yang, E.S.G. Choo, J.M. Xue, D.D. Fan, J. Ding, Optimization of surface coating on Fe3O4 nanoparticles for high performance magnetic hyperthermia agents, J. Mater. Chem. 22 (2012) 8235–8244, https://doi.org/10.1039/C2JM30472D.
[35] C. Boyer, M.R. Whittaker, V. Bulmus, J. Liu, T.P. Davis, The design and utility of polymer-stabilized iron-oxide nanoparticles for nanomedicine applications, NPG Asia Mater. 2 (2010) 23–30, https://doi.org/10.1038/asiamat.2010.6.
[36] A. Mukhopadhyay, N. Joshi, K. Chattopadhyay, G. De, A facile synthesis of PEG-coated magnetite (Fe3O4) nanoparticles and their prevention of the reduction of cytochrome C, ACS Appl. Mater. Interfaces 4 (2012) 142–149, https://doi.org/10.1021/am201166m.
[37] L. Vayssières, C. Chanéac, E. Tronc, J.P. Jolivet, Size tailoring of magnetite particles formed by aqueous precipitation: an example of thermodynamic stability of nanometric oxide particles, J. Colloid Interface Sci. 205 (1998) 205–212, https://doi.org/10.1006/jcis.1998.5614.
[38] L. Kuhrts, E. Macías-Sánchez, N.V. Tarakina, A.M. Hirt, D. Faivre, Shaping magnetite with poly- l -arginine and pH: from small single crystals to large mesocrystals, J. Phys. Chem. Lett. 10 (2019) 5514–5518, https://doi.org/10.1021/acs.jpclett.9b01771.
[39] J.-P. Jolivet, C. Froidefond, A. Pottier, C. Chanéac, S. Cassaignon, E. Tronc, P. Euzen, Size tailoring of oxide nanoparticles by precipitation in aqueous medium. A semi-quantitative modelling, J. Mater. Chem. 14 (2004) 3281–3288, https://doi.org/10.1039/B407086K.
[40] T. Prozorov, S.K. Mallapragada, B. Narasimhan, L. Wang, P. Palo, M. Nilsen-Hamilton, T.J. Williams, D.A. Bazylinski, R. Prozorov, P.C. Canfield, Protein-mediated synthesis of uniform superparamagnetic magnetite nanocrystals, Adv. Funct. Mater. 17 (2007) 951–957, https://doi.org/10.1002/adfm.200600448.
[41] A. Peigneux, Y. Jabalera, M.A.F. Vivas, S. Casares, A.I. Azuaga, C. Jimenez-Lopez, Tuning properties of biomimetic magnetic nanoparticles by combining magnetosome associated proteins, Sci. Rep. 9 (2019) 8804, https://doi.org/10.1038/s41598-019-45219-7.
[42] C. Valverde-Tercedor, M. Montalbán-López, T. Perez-Gonzalez, M.S. Sanchez-Quesada, T. Prozorov, E. Pineda-Molina, M.A. Fernandez-Vivas, A.B. Rodriguez-Navarro, D. Trubitsyn, D.A. Bazylinski, C. Jimenez-Lopez, Size control of in vitro synthesized magnetite crystals by the MamC protein of Magnetococcus marinus strain MC-1, Appl. Microbiol. Biotechnol. 99 (2015) 5109–5121, https://doi.org/10.1007/s00253-014-6326-y.
[43] Y. Liu, Y. Gan, C. Zhao, J. Yang, H. Zhu, Y. Li, S. Shuai, J. Hao, Shaping magnetite by hydroxyl group numbers of small molecules, Langmuir 37 (2021) 5582–5590, https://doi.org/10.1021/acs.langmuir.1c00424.
[44] L. Norfolk, K. Kapusta, D. Cooke, S. Staniland, Ethylenediamine series as additives to control the morphology of magnetite nanoparticles, Green Chem. 23 (2021) 5724–5735, https://doi.org/10.1039/D1GC01539G.
[45] S. Mosivand, Effect of mineral additives on magnetite nanoparticles prepared in an electrolytic cell, Adv. Powder Technol. 32 (2021) 432–444, https://doi.org/10.1016/j.apt.2020.12.020.
[46] R.J. Davey, P.T. Cardew, The kinetics of solvent-mediated phase transformations, Proc. R. Soc. Lond. 398 (1985) 415–428.
[47] C.L. Altan, J.J.M. Lenders, P.H.H. Bomans, G. de With, H. Friedrich, S. Bucak, N.A.J.M. Sommerdijk, Partial oxidation as a rational approach to kinetic control in bioinspired magnetite synthesis, Chem. Eur. J. 21 (2015) 6150–6156, https://doi.org/10.1002/chem.201405973.
[48] K. An, G.A. Somorjai, Size and shape control of metal nanoparticles for reaction selectivity in catalysis, ChemCatChem 4 (2012) 1512–1524, https://doi.org/10.1002/cctc.201200229.
[49] H.-G. Liao, D. Zherebetskyy, H. Xin, C. Czarnik, P. Ercius, H. Elmlund, M. Pan, L.-W. Wang, H. Zheng, Facet development during platinum nanocube growth, Science 345 (2014) 916–919, https://doi.org/10.1126/science.1253149.
[50] J. Baumgartner, M. Antonietta Carillo, K.M. Eckes, P. Werner, D. Faivre, Biomimetic magnetite formation: from biocombinatorial approaches to mineralization effects, Langmuir 30 (2014) 2129–2136, https://doi.org/10.1021/la404290c.
[51] M. Usman, M. Abdelmoula, P. Faure, C. Ruby, K. Hanna, Transformation of various kinds of goethite into magnetite: effect of chemical and surface properties, Geoderma 197-198 (2013) 9–16, https://doi.org/10.1016/j.geoderma.2012.12.015.
[52] C.M. Hansel, S.G. Benner, S. Fendorf, Competing Fe(II)-induced mineralization pathways of Ferrihydrite, Environ. Sci. Technol. 39 (2005) 7147–7153, https://doi.org/10.1021/es050666z.